Microstructure and mechanical behaviors of tibia for collagen-induced arthritic mice treated with gingiva-derived mesenchymal stem cells

Yuxiao Zhou [a], Junlong Dang [b], Ye Chen [c], Song Guo Zheng [c], Jing Du [a],*

[a] *Department of Mechanical Engineering, Pennsylvania State University, University Park, PA, USA*
[b] *Department of Clinical Immunology, Third Affiliated Hospital at the Sun Yat-sen University, Guangzhou, China*
[c] *Division of Rheumatology and Immunology, Department of Internal Medicine at Ohio State University of Medicine and Wexner Medical Center, Columbus, OH, USA*

A R T I C L E   I N F O

A B S T R A C T

Rheumatoid arthritis (RA) is a systemic polyarticular arthritis that primarily affects the small joints but also causes bone erosion in large joints. None of the currently existing treatment approaches is curable. In this study, the effects of human gingiva-derived mesenchymal stem cells (GMSCs) on collagen-induced arthritis (CIA) mice are examined by experimentally assessing the microstructure and mechanical behaviors of tibia. Bone morphology and mineral density of mouse tibiae were assessed using micro-X-ray computed tomography (micro-CT). Compression testing was performed on mouse tibia to access its stiffness. The deformation and strain localized inside proximal tibia were mapped using mechanical testing coupled with micro-CT and digital volume correlation of micro-CT images. The results show that CIA disease caused bone erosion in epiphyseal cortical bone, which manifested into the adjacent epiphyseal trabecular bone, and also affected the metaphyseal cortical bone. CIA disease also weakened the load-bearing function of proximal tibia. GMSC treatment interfered with the progress of CIA, attenuated the bone erosion in epiphyseal and metaphyseal trabecular bone and resulted in improved load-bearing function of proximal tibia. GMSCs provide a promising potential treatment of autoimmune arthritis.

1. Introduction

Rheumatoid arthritis (RA) is an autoimmune disease affecting more than 1.3 million people in the United States (Helmick et al., 2008), with a female/male ratio of 2.5/1 (Lee and Weinblatt, 2001). It causes chronic inflammation of the joints, which may lead to bone erosion in small joints as well as large joints (Firestein, 2003), including knees and shoulders (Schett and Gravallese, 2012; Lee and Choi, 2012; Lindqvist, 2002; Perhala et al., 1991; Clarke et al., 2016; Kirwan et al., 1994; Hermann et al., 2003; Rittmeister and Kerschbaumer, 2001; Kelly et al., 1987). Bone erosions represent localized bone loss, initially involving breaks in the cortical bone surface, then often accompanied by destruction of the adjacent trabecular bone. Bone erosions result from the imbalance in bone remodeling activities, including the excessive bone resorption by osteoclasts and inadequate bone formation by osteoblasts (Schett and Gravallese, 2012).

RA patients are treated with disease-modifying antirheumatic drugs (DMARDs), non-steroidal anti-inflammatory drugs (NSAIDs) and glucocorticoids. Although some currently existing treatments inhibit both bone erosion and inflammation, repair of existing bone lesions rarely occurs (Schett and Gravallese, 2012). Lack of repair is partly due to proinflammatory cytokines that suppress bone formation (Schett and Gravallese, 2012). Although these treatments are favorable for most patients, they may be associated with serious long-term side effects. More importantly, none of them is curative (Firestein, 2003; Aletaha and Smolen, 2018). Therefore, new treatment approaches are still urgently needed.

Substantial evidence exists that naturally occurring regulatory T cells (nTreg) play an important role in the prevention of autoimmune diseases including RA (Sakaguchi et al., 2008; Zhou et al., 2010; Frey et al., 2010). However, it is challenging to stabilize nTregs in the inflammatory condition and to maintain their functionality (Chen et al., 2020). Unlike nTreg, induced Treg cells (iTreg) are stable and functional in conditions with inflammation (Lan et al., 2012; Zheng et al., 2004a, 2004b). We've previously demonstrated that infusion of human gingiva-derived mesenchymal stem cells (GMSCs) enhanced iTreg cells differentiation

and down-regulated inflammatory cytokine production in collagen-induced arthritis (CIA) mice (Chen et al., 2013), a mice model that shares many common features with rheumatoid arthritis (Trentham et al., 1977). We've previously shown that histopathological evaluation on bone/cartilage destruction suggested a significant delay in arthritis onset and a decrease in arthritis severity after adoptive transfer of GMSCs (Chen et al., 2013). In our prior work, micro X-ray computed tomography (micro-CT) evaluation showed the bone volumes of metatarsophalangeal joints were significantly higher in GMSC-treated mice than those in the CIA mice (Luo et al., 2019).

The load-bearing function of bone upon CIA disease and GMSCs treatment has never been explored. The structure-function relationship in GMSC-treated CIA mice bone is not clear either. This study aims at investigating the load-bearing functional responses of GMSC-treated CIA mouse tibia and its relationship with the changes in bone microstructure. In this work, CIA mice were treated with GMSCs. Bone mineral density and microstructures in tibiae were assessed based on micro-CT imaging. The mechanical behaviors of tibiae were characterized by compression testing. The localized micro-scale deformation and strain inside proximal tibia were mapped using mechanical testing coupled with micro-CT. The effects of GMSC treatment on the form and function of CIA tibia bone were discussed.

2. Materials and methods

2.1. Sample preparation

The following animal work has been approved by the Institutional Animal Care and Use Committee (IACUC) of Penn State University and Ohio State University, respectively. All experimental procedures were conducted in compliance with the ARRIVE guidelines and National Institutes of Health (NIH) Guide for Care and Use of Laboratory Animals. The details of arthritis induction and GMSC treatment are described in our prior publication (Chen et al., 2013). Female FoxP3^{gfp} reporter DBA/1J mice (Jackson Laboratory, Bar Harbor, ME) were bred at the Penn State University and Ohio State University. All mice were maintained and handled under specific-pathogen-free (SPF) conditions according to the IACUC and facilities guidelines approved in each of the respective institutes. All mice were fed with LabDiet® 5K52 formulation (6% fat) and housed under corncob granules condition.

At week 8, all mice were randomly divided into four groups. One group didn't receive any injection (unoperated control group, n = 9), whereas collagen induced arthritis (CIA) was induced in other three groups via immunization of type II collagen (emulsified in Complete Freund adjuvant, 100 µg/mouse). One of these three groups didn't receive any injection after inducing arthritis (CIA group, n = 15). Two weeks after arthritis induction, gingival tissue-derived mesenchymal stem cells (GMSCs) were infused into a group of mice by single intravenous injection of 2×10^6 GMSCs for each mouse (GMSCs-treated group, n = 15) (Chen et al., 2013). Alternatively, a similar dose of human dermal fibroblasts (American Type Culture Collection, Manassas, VA) was injected intravenously into a group of mice (negative control group, n = 10) (Chen et al., 2013).

In another 6 weeks, all four groups of mice were sacrificed. Tibiae were collected with all soft tissue and fibulae carefully removed. Tibia specimens were first wrapped in Kimwipe (Kimberly-Clark, Irving, TX) soaked with modified Hanks' Balanced Salt Solution (HBSS) (Sigma Aldrich, St. Louis, MO), and then wrapped in parafilm to prevent dehydration. They were kept frozen at −23 °C, until 12 h prior to the following testing, when they were thawed in fridge.

2.2. Bone mineral density assessment

All tibia specimens were scanned in a micro-CT (Phoenix v|tome|x L300, GE, Boston, MA) with 100 kV voltage, 120 µA current, 285 kVp X-ray tube peak potential peak, 200 ms integration time per projection and

frame averaging of 3. The specimens were wrapped in Kimwipe soaked with HBSS. Micro-CT images of proximal tibia together with tibial shaft were obtained (Fig. 1). The isometric voxel size was 12 µm. Each micro-CT image stack was segmented using the watershed algorithm in an image analysis software (Avizo, FEI Visualization Sciences Group, Burlington, MA), with the same threshold across specimens for consistency. The proximal epiphyseal region spanned from the proximal tibial plateau to the growth plate. The metaphyseal region started from the growth plate and extended 1.2 mm proximally. The diaphyseal region started where the metaphyseal region ends and extended to the distal-diaphysis, i.e. at 75% length of tibia. In the epiphyseal and metaphyseal regions, respectively, trabecular bone region was identified as an irregular anatomic region of interest drawn manually a few voxels away from the endocortical boundary. In each region of interest, bone tissue was further segmented from marrow and soft tissue (Fig. 1).

The micro-CT scanner was calibrated using a hydroxyapatite (HA) phantom that contains five cylindrical inserts with various HA concentrations (PHA-33, QRM, Möhrendorf, Germany). The tissue mineral density (TMD) for epiphyseal, metaphyseal and diaphyseal cortical bone, and epiphyseal and metaphyseal trabecular bone were estimated using the segmented micro-CT images, respectively. Bone mineral density (BMD) for the epiphyseal and metaphyseal trabecular bone were estimated, respectively (Bouxsein et al., 2010). TMD was calculated for the bone tissue only; whereas BMD was calculated by including the void spaces among trabecular bone.

2.3. Bone microstructure assessment

The bone microstructures were assessed based on the recommendations provided by Bouxsein et al. (2010). For the cortical bone in three regions of interest (epiphysis, metaphysis and diaphysis), total cross-sectional area inside the periosteal envelope (Tt.Ar), cortical bone area (Ct.Ar) were assessed, respectively using Avizo (Bouxsein et al., 2010). Besides these commonly used morphometric indices, two indices commonly used in materials science were adopted. It has been reported that bone surface roughness increased after CIA induction (Silva et al., 2006). As an indicator of surface roughness, the surface curvature,
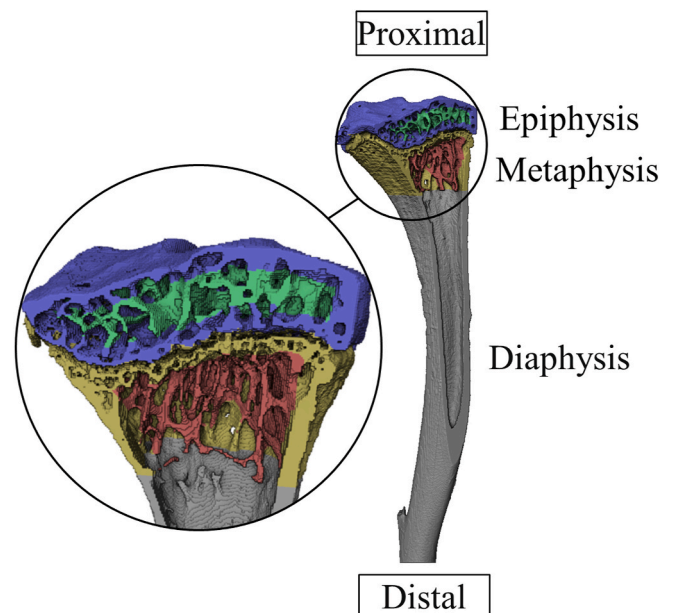
Fig. 1. 3D rendering of a representative micro-CT image stack virtually sectioned frontally to show the segmentation of bone tissues in different regions of interest: Blue – Epiphyseal cortical bone; Green – Epiphyseal trabecular bone; Yellow – Metaphyseal cortical bone; Red – Metaphyseal trabecular bone; Grey – Diaphyseal cortical bone.

defined by Bhushan (2000), was calculated for the proximal tibial plateau surfaces using Avizo. Surface-to-volume ratio (SA/V), which is given by surface area divided by volume (Ott, 2018), was also calculated using Avizo.

For the epiphyseal and metaphyseal trabecular bone, the bone volume fraction (BV/TV), mean trabecular thickness (Tb.Th), connectivity density (Conn.D) were calculated using BoneJ plug-ins (Doube et al., 2010) in ImageJ software (National Institute of Health, Maryland, USA) (Bouxsein et al., 2010; Dougherty and Kunzelmann, 2007).

2.4. Mechanical testing

Tibia specimens were partially embedded from distal end to 70% of total height in polymethyl methacrylate (PMMA) (Ortho-Jet BCA, Lang Dental, Wheeling, IL). A small amount of PMMA was fixed on top of the proximal tibial plateau to create a flat surface for better load transfer in the subsequent mechanical testing (Fig. 2). The PMMA dough did not infiltrate into the tibial plateau during this process, which was confirmed by the micro-CT images taken in section 2.5. During testing, tibia specimens were wrapped in Kimwipe soaked with HBSS to avoid dehydration (Fig. 2).

Compression testing was performed in a mechanical tester (Electro-Puls E3000, Instron, Norwood, MA). A compressive load was applied on the PMMA on top of the proximal tibial plateau at a constant displacement rate of 0.1 mm/min until the load reached 5 N, then it was unloaded. After 8-min relaxation at no load condition, the tibia specimen was loaded again. Five loading cycles were repeated for each tibia specimen, to check the consistency in the recorded load-displacement curves. The stiffness of each tibia specimen was obtained by calculating the slope for part of the load-displacement curve from the peak load of 2.5 N–5 N. Statistical significance ($p < 0.05$) in the stiffness values across the four groups were evaluated using Tuckey pair-wise comparison in Minitab software. No outlier removal was applied.

2.5. Mechanical testing coupled with micro-CT

One tibia specimen was selected from each group, so that its stiffness being the closest to mean stiffness in the group. Compression testing was performed on the selected specimens in a loading stage (CT5000, Deben, Suffolk, UK) coupled with micro-CT scanner (Fig. 2). A compressive load was applied on the PMMA on top of proximal tibial plateau at a constant displacement rate of 0.1 mm/min until the load reached to 5N. The load was held at 5N for 1 h until the change of loading fixture position over time was minimal. Micro-CT scans were performed before loading and after 1-hr holding, respectively, using a voltage of 100 kV and a current of 100 μA. Each scan took approximately 30 min. Micro-CT images with isometric voxel size of 10 μm were obtained.

3D full-field displacement field inside the proximal tibia was calculated using digital volume correlation (DVC) of micro-CT images at no-load and loaded conditions in DaVis software (LaVision, Goettingen, Germany). The background images (air, embedding materials, etc.) were masked and only the correlation windows that contain more than 10% valid voxels were used in the correlation. Multiple passes of correlation were carried out with reducing isometric correlation window size. The correlation window size in the last pass was 160 μm. The overlap between adjacent correlation windows was 50%. Displacement vectors with correlation value below 0.8 or peak ratio below 1.5 were removed from the results and replaced by interpolation of neighboring vectors.

To eliminate the effects of rigid body movement when comparing the deformation inside proximal tibia, the images were rigidly translated, so that the distal end of proximal tibia was aligned in the loaded and no-load images. 3D full-field strain field inside proximal tibia was calculated by the numerical differentiation of displacement field. The measured 3D displacement and strain fields in the proximal tibia were mapped on to the bone microstructures by 3D rendering in Avizo. Average and standard deviation were calculated. Statistical analysis was not performed. The noise in the results was estimated by DVC of two stacks of micro-CT images both taken at no-load conditions for the same specimen.

2.6. Statistical analysis

Data was presented as mean ± standard deviation (SD). The sample size estimation was conducted from preliminary data including unoperated control and CIA groups. Statistical significance ($p < 0.05$) in the above-mentioned mineral density, morphological indices, stiffness of tibia across the four groups were evaluated using Tuckey pair-wise comparison in Minitab software (Minitab, LLC, State College, PA). No outlier removal was applied.
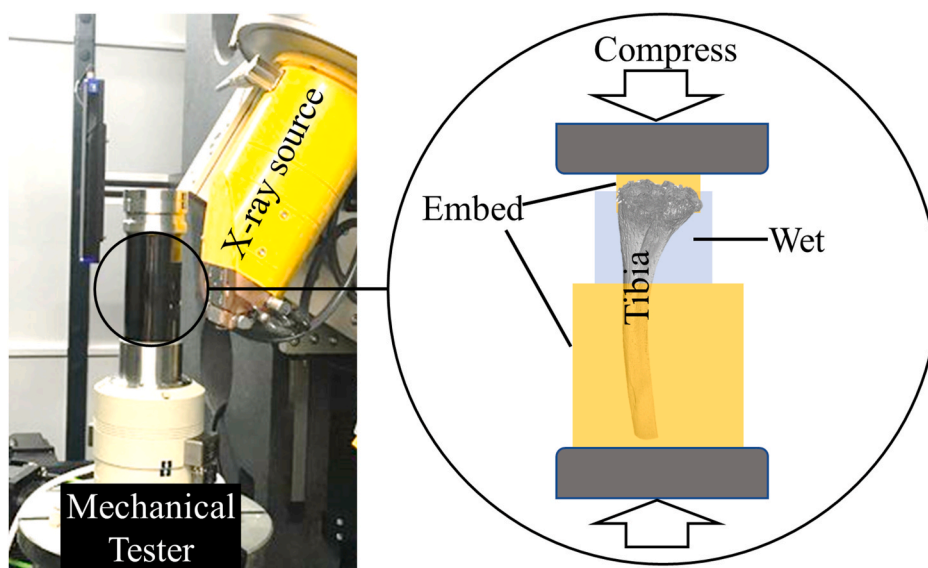
Fig. 2. Schematic of the compression testing on mice tibia coupled with micro-CT.

3. Results

3.1. Bone mineral density

The bone mineral density values measured from micro-CT images are presented in Fig. 3, as well as Tables 1 and 2. The TMD for cortical bone was not significantly different among 4 groups, in epiphysis (Fig. 3a), metaphysis (Fig. 3d) or diaphysis (Fig. 3g). The TMD for the epiphyseal trabecular bone in CIA mice was lower than those in the unoperated control, but not significantly different between other pairs (Fig. 3b). The BMD for epiphyseal trabecular bone in the CIA group and in the negative control was lower than that in the unoperated control. The BMD for epiphyseal trabecular bone in the GMSC-treated group was 31.9% higher than that in the negative control (Fig. 3c). The TMD for the metaphyseal trabecular bone in the CIA mice was lower than those in the unoperated control but was not significantly different between other pairs (Fig. 3e). The BMD for metaphyseal trabecular bone in the GMSC-treated CIA mice was significantly higher (27.4%) than that in the CIA mice (Fig. 3f).

3.2. Bone morphometry

The bone morphometric indices measured for the tibia epiphysis are presented in Fig. 4, as well as Tables 1 and 2 The Tt.Ar for cortical bone was not significantly different among 4 groups (Fig. 4a). The Ct.Ar for cortical bone, the BV/TV and Tb.Th for trabecular bone in the CIA mice were lower than those in the unoperated control (Fig. 4bde). Same trends were also observed when comparing negative control with the unoperated control for Ct.Ar, BV/TV, Tb.Th (Fig. 4bde). The Ct.Ar in the GMSC-treated group were 23.7% higher than those in the negative control (Fig. 4bd). The BV/TV in the GMSC-treated group were 71.7%

higher than those in the negative control (Fig. 4bd). The SA/V for cortical bone in the CIA mice and negative control were higher than that in the unoperated control (Fig. 4c). The SA/V for GMSC-treated mice was 20.0% lower than that in the negative control (Fig. 4c). The Conn.D for the trabecular bone in GMSC-treated CIA mice was 73.0% higher than that in the CIA mice and 78.5% higher than that in the negative control (Fig. 4f). The surface curvature was significantly different between any of the two groups among the four groups (Table 1). The erosions in epiphyseal cortical bone can also be visually observed in Fig. 4g in the CIA mice and the negative control.

The bone morphometric indices measured for the tibia metaphysis are presented in Fig. 5 as well as Tables 1 and 2 For the cortical bone, the Tt.Ar for unoperated control was significantly higher than those for the other three groups (Fig. 5a). The Ct.Ar for unoperated control was higher than negative control. The SA/V for GMSC-treated CIA mice was significantly lower (17.9%) than that for the negative control. For the trabecular bone, the BV/TV was not significantly different among 4 groups. The Tb.Th for negative control was significantly lower than those for the unoperated control (20.1%) and the GMSC-treated mice (16.8%). The Conn.D for GMSC-treated mice was significantly higher than those for the CIA mice (78.5%) and negative control (81.0%).

The bone morphometric indices measured for the tibia diaphysis are presented in Fig. 6 as well as Table 1. No significant difference was observed in any of the morphometric indices (Tt.Ar, Ct.Ar and SA/V) among the 4 groups.

3.3. Mechanical behaviors

The load-displacement curves were recorded for all specimens during the 5 cycles of compression test. The one specimen that had its stiffness being the closest to the mean stiffness in its group was chosen as
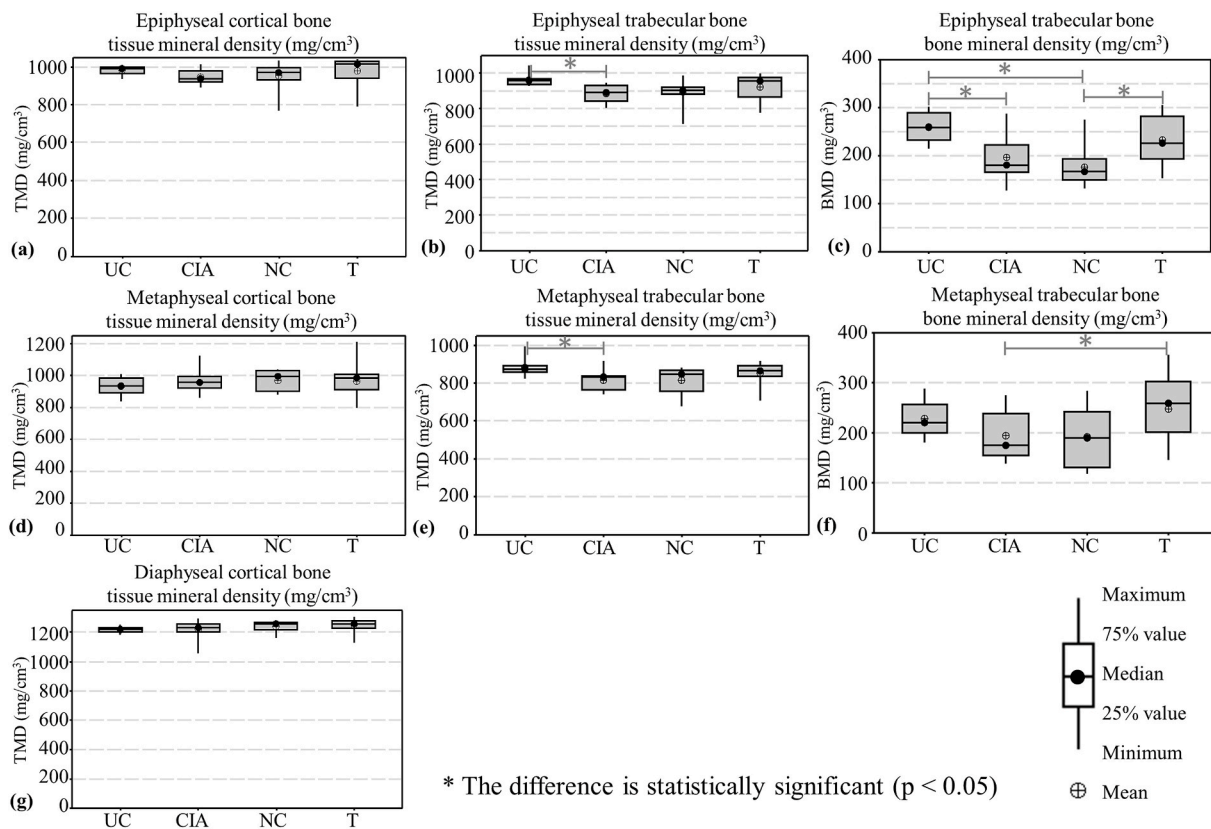
Fig. 3. The TMD and BMD in different regions of mouse tibia. (a) TMD in epiphyseal cortical bone, (b) and (c) TMD and BMD in epiphyseal trabecular bone, (d) TMD in metaphyseal cortical bone, (e) and (f) TMD and BMD in metaphyseal trabecular bone, (g) TMD in diaphyseal cortical bone. UC – Unoperated control; CIA – Collagen-induced arthritis mice; NC – Negative control; T – GMSC-treated CIA mice.

Table 1
Tissue mineral density and morphometric indices of cortical bone in the three regions of interest in tibia for the 4 groups of mice: UC – Unoperated control; CIA – Collagen-induced arthritis mice; NC – Negative control; T – GMSC-treated CIA mice.

	Index	UC	CIA	NC	T
Epiphysis	TMD (mg/cm³)	981.5 ± 24.11	948.6 ± 35.92	953.4 ± 73.6	979.7 ± 67.9
	Tt.Ar (mm²)	2.44 ± 0.21	2.22 ± 0.24	2.24 ± 0.36	2.16 ± 0.23
	Ct.Ar (mm²)	1.18 ± 0.2^{ab}	0.93 ± 0.2^{a}	0.82 ± 0.13^{bf}	1.02 ± 0.11^{f}
	SA/V (mm⁻¹)	14.16 ± 1.84^{ab}	16.87 ± 3.15^{a}	19.01 ± 2.79^{bf}	15.21 ± 2.84^{f}
	Surface Curvature (mm⁻¹)	46.85 ± 23.58^{abc}	55.72 ± 31.48^{ade}	53.62 ± 30.25^{bdf}	49.15 ± 25.16^{cef}
Metaphysis	TMD (mg/cm³)	934.5 ± 55.4	957.2 ± 65.8	969.9 ± 66.1	965.0 ± 104.0
	Tt.Ar (mm²)	4.13 ± 0.41^{abc}	3.47 ± 0.27^{a}	3.60 ± 0.40^{b}	3.41 ± 0.27^{c}
	Ct.Ar (mm²)	0.042 ± 0.006^{b}	0.035 ± 0.007^{b}	0.032 ± 0.006	0.034 ± 0.009
	SA/V (mm⁻¹)	8.03 ± 0.57	7.90 ± 1.43	8.79 ± 1.25^{f}	7.22 ± 0.87^{f}
Diaphysis	TMD (mg/cm³)	1220.2 ± 21.1	1220.6 ± 57.4	1241.8 ± 35.8	1252.0 ± 41.4
	Tt.Ar (mm²)	1.09 ± 0.16	0.91 ± 0.08	0.97 ± 0.09	0.95 ± 0.15
	Ct.Ar (mm²)	0.71 ± 0.12	0.60 ± 0.14	0.61 ± 0.08	0.64 ± 0.12
	SA/V (mm⁻¹)	7.29 ± 0.34	7.69 ± 0.62	7.68 ± 0.87	7.18 ± 0.84

a - Significant differences between UC and CIA; b - Significant differences between UC and NC; c - Significant differences between UC and T; d – Significant differences between CIA and NC; e – Significant differences between CIA and T; f – Significant differences between NC and T.

Table 2
Bone mineral density and morphometric indices of trabecular bone in the proximal tibia for the 4 groups of mice: UC – Unoperated control; CIA – Collagen-induced arthritis mice; NC – Negative control; T – GMSC-treated CIA mice.

	Index	UC	CIA	NC	T
Epiphysis	TMD (mg/cm³)	961.2 ± 34.8^{a}	885.6 ± 48.8^{a}	893.4 ± 70.2	922.8 ± 70.8
	BMD (mg/cm³)	260.3 ± 31.0^{ab}	196.9 ± 43.2^{a}	176.5 ± 40.8^{bf}	232.8 ± 51.0^{f}
	BV/TV (%)	18.26 ± 3.80^{ab}	11.65 ± 5.01^{a}	8.95 ± 4.49^{bf}	15.37 ± 5.21^{f}
	Tb.Th (μm)	62.22 ± 6.12^{ab}	53.98 ± 7.35^{a}	50.85 ± 9.47^{b}	53.87 ± 6.44
	Conn.D (mm⁻³)	148.9 ± 43.9	110.5 ± 73.4^{e}	107.1 ± 77.4^{f}	191.2 ± 55.0^{ef}
Metaphysis	TMD (mg/cm³)	883.0 ± 46.5^{a}	816.1 ± 52.4^{a}	817.2 ± 68.4	855.1 ± 52.5
	BMD (mg/cm³)	228.6 ± 35.0	194.6 ± 49.3^{e}	192.5 ± 58.0	248.0 ± 64.6^{e}
	BV/TV (%)	16.04 ± 4.59	12.49 ± 6.50	11.82 ± 7.26	18.79 ± 7.8
	Tb.Th (μm)	50.71 ± 5.81^{b}	45.65 ± 6.39	40.07 ± 4.62^{bf}	48.14 ± 4.97^{f}
	Conn.D (mm⁻³)	67.63 ± 24.4	57.20 ± 39.8^{e}	56.4 ± 43.6^{f}	102.1 ± 46.9^{ef}

a - Significant differences between UC and CIA; b - Significant differences between UC and NC; c - Significant differences between UC and T. d – Significant differences between CIA and NC; e – Significant differences between CIA and T; f – Significant differences between NC and T.

the representative specimen for the group. Curves for one representative specimen in GMSC-treated group are presented in Fig. 7a. As it shows in Fig. 6a, the curves are very similar to each other, especially those

recorded during the 2nd to the 5th cycles, which was also true for other specimens. All specimens exhibited high repeatability in the compressive test. Hence, the load-displacement curves recorded in the 5th loading cycle are presented in Fig. 7b.

The load-displacement relationships were nonlinear (Fig. 7b). The stiffness increased with increasing load. The stiffness values of all specimens were calculated for the second part of the curves and summarized in the boxplot in Fig. 7c. The stiffness values of the CIA mice spanned a wider range than those of the other 3 groups. The lower bound of stiffness values for the CIA mice was also the lowest among the 4 groups. The GMSCs-treated mice had significantly higher (52.1%) stiffness than the CIA mice.

For each representative specimen in its group, the 3D full-field axial deformation and axial strain, respectively, measured in the mechanical testing coupled with micro-CT are presented in the animations in the supplemental materials. The axial deformation distributions on the frontal sections through the center of the tibia specimens were presented in Fig. 8a. The 3D rendered images were virtually sectioned to display the internal deformation distribution. The average deformation measured in 3D bone microstructures were calculated. The axial deformation towards the loading direction in proximal tibia of the CIA mouse (46.3 ± 30.8 μm) and negative control mouse (37.5 ± 25.9 μm) were much greater than that of unoperated control (4.07 ± 2.61 μm). For the GMSCs-treated mouse, the deformation in proximal tibia (14.0 ± 8.68 μm) was smaller than that of CIA mouse and negative control, and the variation was also smaller.

The axial strains in proximal tibiae measured from the mechanical testing coupled with micro-CT were all in compression. The 3D full-field strain maps in the proximal tibiae are presented in the video clip in the supplemental content. The strain distribution on the same frontal sections were presented in Fig. 8b. Although strain ranges were different between groups, the strain distribution patterns were similar, with high strain concentration around the growth plates. The average strain measured in 3D bone microstructures were calculated. The axial strain of the CIA mouse (−1.263 ± 0.722%) and the negative control (−1.050 ± 0.629%) were greater than that of unoperated control (−0.344 ± 0.357%). For the GMSCs-treated mouse, axial strain (−0.396 ± 0.343%) was smaller than those in the CIA mouse and negative control.

The distributions of maximum principal strain on the same frontal sections were presented in Fig. 8c. The average maximum principal strain measured in 3D bone microstructures for the CIA mouse (1.644 ± 0.922%) and the negative control (1.448 ± 0.799%) were greater than that of unoperated control (0.149 ± 0.068%). For the GMSCs-treated mouse, average strain (0.152 ± 0.129%) was smaller than those in the CIA mouse and negative control.

The distributions of minimum principal strain on the same frontal sections were presented in Fig. 8d. The average strain measured in 3D bone microstructures for the CIA mouse (−1.625 ± 2.263%) and the negative control (−1.541 ± 1.877%) were lower than that of unoperated control (−0.361 ± 0.269%). For the GMSCs-treated mouse, average strain (−0.477 ± 0.427%) was higher than those in the CIA mouse and negative control.

Using the zero-load method, the noise in the measured displacement was estimated to be 0.3 μm and the measured strain was estimated to be 0.02%, 0.06% and 0.16% for axial strain, maximum principal strain and minimum principal strain.

4. Discussion

The results of this study show the changes in the form (bone morphology) and in the function (load-bearing) of mouse tibia due to CIA and due to GMSC-based treatment. The form-function relationship is also discussed for GMSC-treated CIA mice.
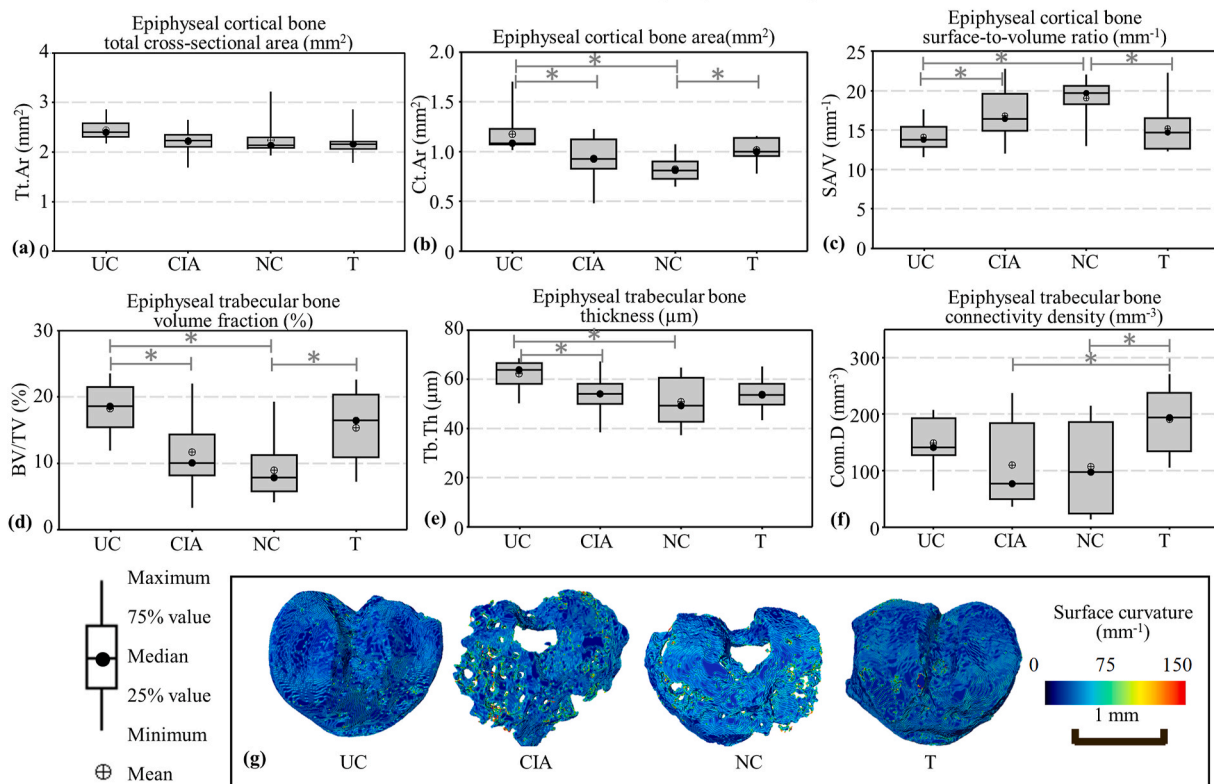
Fig. 4. Microstructure assessment for the epiphysis. (a) Total cross-sectional area, (b) bone area and (c) surface-to-volume ratio for epiphyseal cortical bone. (d) Bone volume fraction, (e) trabecular thickness and (f) connectivity density for epiphyseal trabecular bone. (g) Surface curvature of proximal tibial plateaus on one typical tibia for each group. UC – Unoperated control; CIA – Collagen-induced arthritis mice; NC – Negative control; T – GMSC-treated CIA mice.

4.1. Effects of CIA on bone morphology and mineral density

CIA mice model shares many common features with rheumatoid arthritis (Trentham et al., 1977) and causes bone erosion at the joints. The results in this study show that the bone destruction caused by CIA was most severe in epiphysis, and was also extend to metaphysis, but had not seriously affected diaphysis yet. It is consistent with the bone erosion development pattern in RA patients in other studies (Schett and Gravallese, 2012).

Bone loss manifested by focal marginal joint erosions represents the radiographic hallmark of RA (Goldring and Gravallese, 2000). In the epiphysis, compared with unoperated control, the CIA mice had smaller cortical bone area (Fig. 4b) and higher surface-area-to-volume ratio (Fig. 4c), which indicates disconnected bone pieces. The surfaces of proximal tibial plateaus were also rougher for CIA mice than those for the unoperated control (Fig. 4g). The results also show that the bone erosion had manifested to epiphyseal trabecular bone, where the CIA mice had lower bone tissue mineral density (Fig. 3b), bone mineral density (Fig. 3c), lower bone volume fraction (Fig. 4d), and smaller trabecular thickness (Fig. 4e) than those for the unoperated control.

The results show that bone destruction caused by CIA has extend to metaphysis, where the total cross-sectional cortical bone area of CIA mice was lower than that of the unoperated control (Fig. 5a), the trabecular tissue mineral density of CIA mice was lower than that of the unoperated control (Fig. 3e). Bone destruction caused by CIA had not seriously affected diaphysis yet, because there was no significant difference between cortical bone in CIA mice and that in the unoperated control, in terms of morphometric indices or mineral densities (Fig. 6).

4.2. Effects of GMSC treatment on bone morphology and mineral density

The results also show that GMSC treatment significantly attenuated the bone erosion for CIA mice. In the epiphysis and metaphysis, the trabecular connectivity density for GMSC-treated CIA mice was significantly higher than that for the CIA mice (Figs. 4f and 5f). In the metaphysis, the trabecular bone mineral density for GMSC-treated mice was significantly higher than that for the CIA mice (Fig. 3f). The surface curvature for proximal tibial plateaus in GMSC-treated mice was 11.8% smaller than that in the CIA mice (Table 1). The difference in epiphyseal cortical bone between the GMSC-treated and CIA groups can also be visually observed in Fig. 4g.

Our previous study showed that the bone volumes of metatarsophalangeal joints were significantly higher in GMSC-treated mice than those in the CIA mice (Luo et al., 2019). This is in good agreement with the findings in this study. Our previous study also demonstrated that GMSC directly inhibit the osteoclasts differentiation by reducing the activities of nuclear factor kappa B (NF-κB) (Luo et al., 2019). The attenuation of bone erosion that we observed in this study can be related to the reduction of osteoclasts in CIA.

Our prior work has shown that fibroblasts express CD73 (ecto-5′-nucleotidase) but not CD39 (nucleoside triphosphate diphosphohydrolase-1, NTPDase 1), hence they did not inhibit T cell proliferation *in vitro* (Chen et al., 2013). In contrast, GMSCs express both CD39 and CD73 (Chen et al., 2013), and co-expression of CD39 and CD73 in Treg cells contribute to its inhibitory function (Deaglio et al., 2007). In this study, the negative control does not have significant difference with CIA mice, in terms of bone mineral density (Fig. 3), bone morphology (Figs. 4–6, Tables 1 and 2) and mechanical properties (Figs. 7 and 8). Therefore, fibroblasts (negative control) do not have a therapeutic effect on CIA.
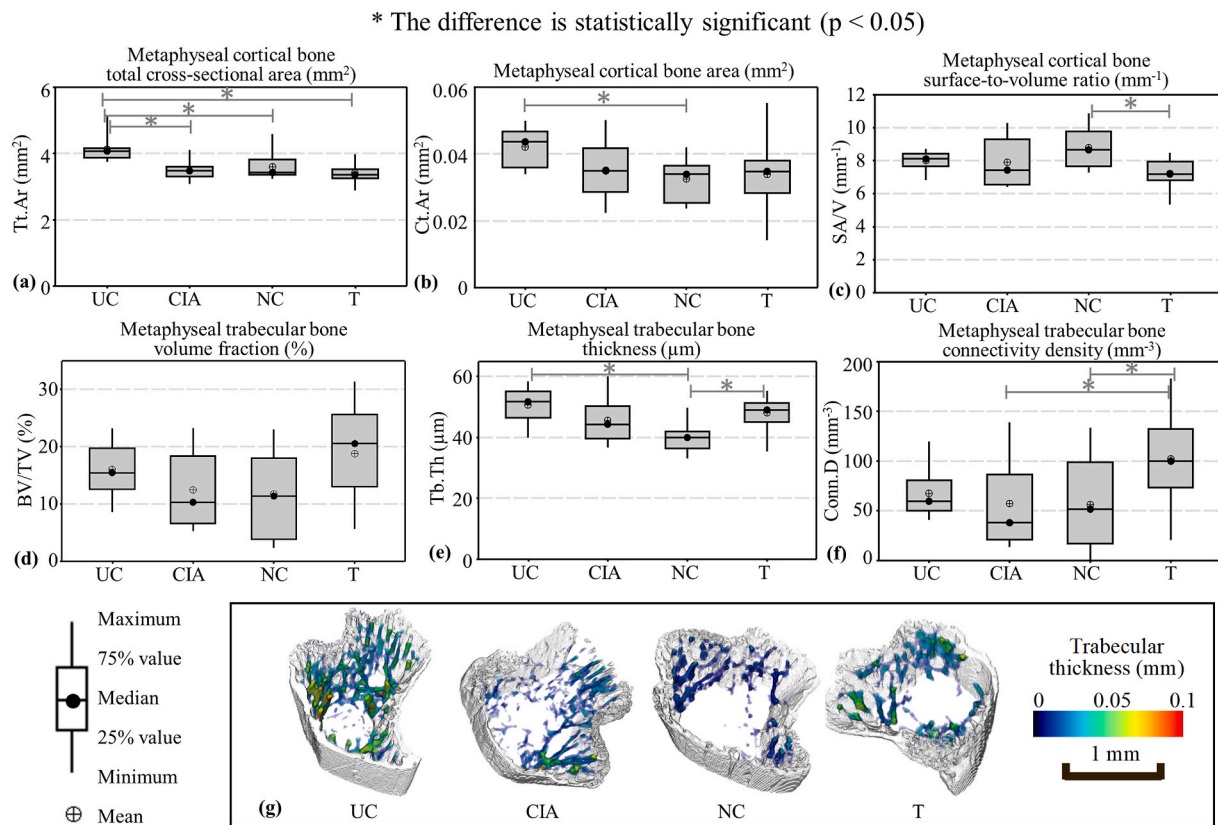
Fig. 5. Microstructure assessment for the metaphysis. (a) Total cross-sectional area, (b) bone area and (c) surface-to-volume ratio for metaphyseal cortical bone. (d) Bone volume fraction, (e) trabecular thickness and (f) connectivity density for metaphyseal trabecular bone. (g) Three-dimensional rendering of metaphyseal trabecular thickness on one typical tibia for each group. UC – Unoperated control; CIA – Collagen-induced arthritis mice; NC – Negative control; T – GMSC-treated CIA mice.
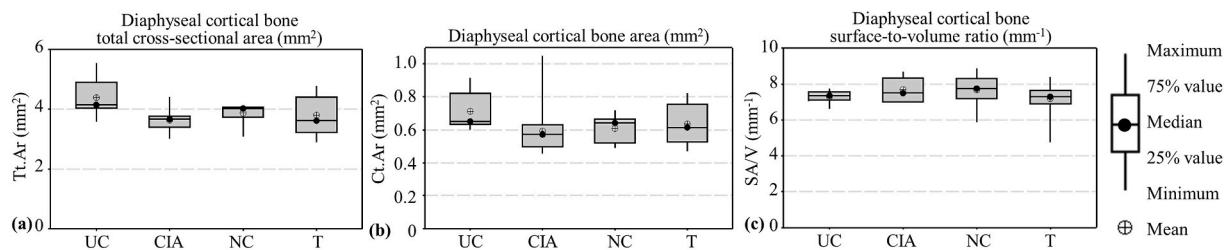
Fig. 6. Microstructure assessment for the diaphysis. (a) Total cross-sectional area, (b) bone area and (c) surface-to-volume ratio for diaphyseal cortical bone. UC – Unoperated control; CIA – Collagen-induced arthritis mice; NC – Negative control; T – GMSC-treated CIA mice.

4.3. Load-bearing function and form-function relationship

The load-bearing function of mouse tibia bone was also affected by CIA and GMSC treatment, respectively. The magnitude of deformation and the magnitude of strain in proximal tibia for CIA mice were greater than those in the unoperated control (Fig. 8), which indicates that the load-bearing function of proximal tibia was weakened due to CIA. The stiffness of tibia for GMSC-treated mice was higher than that for CIA mice (Fig. 7c). The magnitude of deformation and the magnitude of strain in proximal tibia for GMSC-treated mice were smaller than those for CIA mice (Fig. 8). These indicate that the proximal tibia for GMSC-treated mice has better load-bearing function than those for the CIA mice.

The results of this study can also be related to the form-function relationships for mouse tibia. The form (bone morphology) and

function (load-bearing) of proximal tibia were both affected by CIA and then by GMSC-treatment. Compared with normal bone, changes in bone morphology and stiffness of proximal tibia for rheumatoid arthritis patients have been reported in previous literatures. Specially, reduced stiffness in proximal tibia was observed (Lereim et al., 1974; Lereim and Goldie, 1975; Yang et al., 1997), as a result of bone erosion, reduced bone fraction, and fractured trabeculae (Lereim and Goldie, 1975). Consistent with previous studies, the results of this work show that CIA affects several bone morphology indicis in mouse proximal tibia, such as decreased bone volume fraction and reduced trabecular thickness (Figs. 4 and 5, Tables 1 and 2). Moreover, the results also show that CIA reduced tissue mineral density in proximal tibia (Fig. 3). Hence, the reduction in the stiffness for epiphysis and metaphysis can be expected, which lead to the increases in the localized deformation and strain in the proximal tibia (Fig. 8).
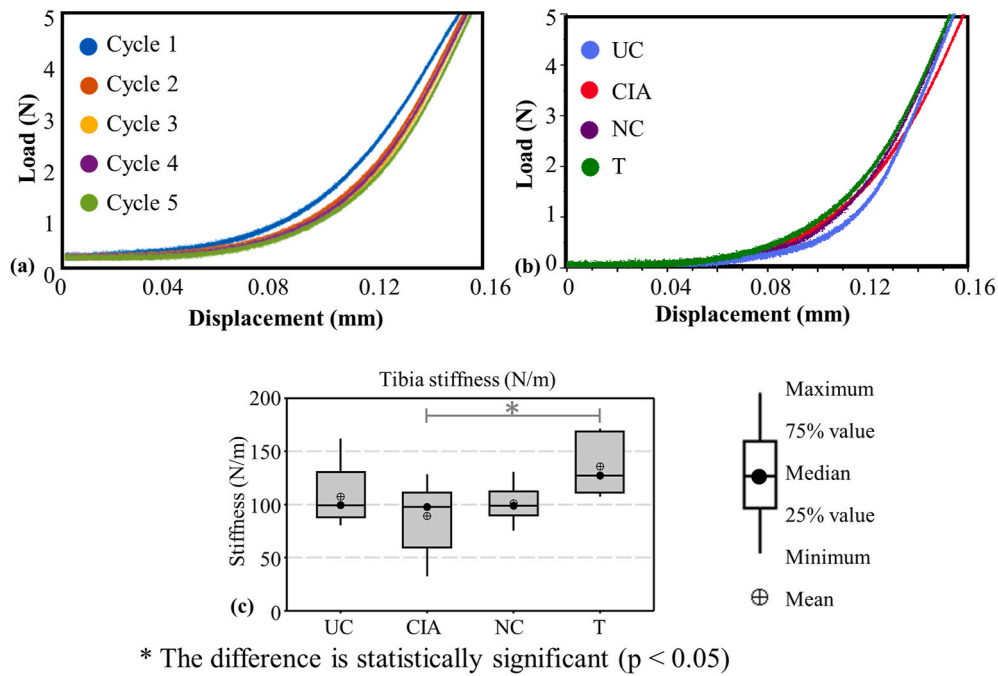
Fig. 7. (a) Load-displacement curves recorded in the 5 repetitive compression cycles for a representative GMSC-treated specimen. (b) Load-displacement curves for a presentative specimen in each group; (c) Comparison of tibia stiffness among groups. UC – Unoperated control; CIA – Collagen-induced arthritis mice; NC – Negative control; T – GMSC-treated CIA mice.
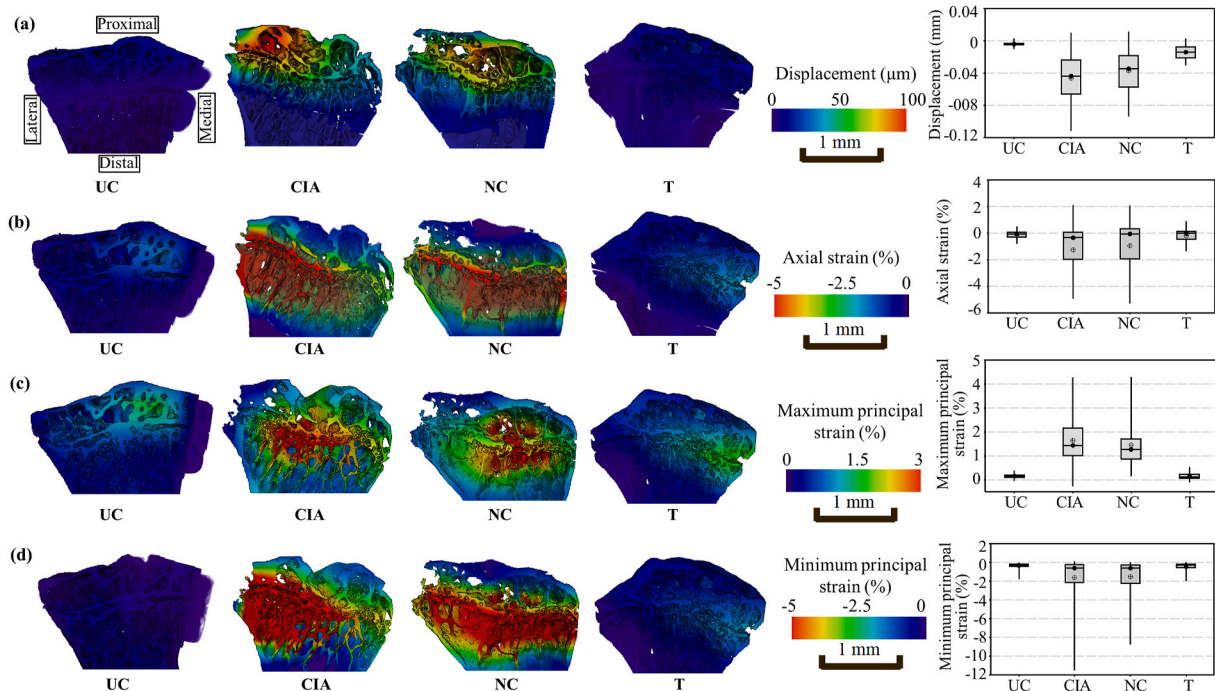
Fig. 8. Three-dimensional rendering and boxplot of (a) axial displacement, (b) axial strain, (c) maximum principal strain and (d) minimum principal strain in proximal tibial plateau for a representative specimen in each group. Rendered images were virtually sectioned to show the displacement and strain distribution on the frontal sections. UC – Unoperated control; CIA – Collagen-induced arthritis mice; NC – Negative control; T – GMSC-treated CIA mice.

Several bone morphometric indicis and bone mineral density in epiphysis and metaphysis showed the attenuation of bone erosion in epiphysis and metaphysis by GMSC treatment (Figs. 3–5, Tables 1 and 2). Though the tissue mineral density was not improved by GMSC treatment (Fig. 3), the increased connectivity density (Figs. 4 and 5) leads to the increased bone mineral density (Fig. 3). This indicated the stiffness of proximal tibia increased after CIA mice received GMSC

treatment. Therefore, the localized deformation and strain in the proximal tibia in the GMSC-treated mice was smaller than those in the CIA mice (Fig. 8).

For the diaphysis, Since the bone morphology and mineral density were not significantly affected by CIA or by GMSC treatment (Figs. 3 and 5), the stiffness of diaphysis should not be affected, either. The stiffness measured in the conventional compression test (Fig. 7) was the

combined stiffness for the epiphysis, metaphysis and diaphysis. No difference in the stiffness were found among groups, except between the CIA mice and GMSC-treated mice. This is different than the discoveries in other studies by Fonseca et al. in which they showed that the bone morphology and stiffness for the diaphysis in other arthritis mice models were both impaired by the disease (Caetano-Lopes et al., 2009; Vidal et al., 2018).

4.4. Advantage, limitation and future works

There are several advantages for the mechanical behavior measurement methods used in current work. Using mechanical testing coupled with micro-CT, the deformation and strain localized inside the epiphysis and metaphysis were measured and their stiffness can be estimated. It is especially important in the study of the diseases that mostly affect the joints of bone, for example the CIA mice model. In comparison, the conventional compression test of tibia that was also performed in this study measured the combined stiffness for the epiphysis, metaphysis and diaphysis. It cannot differentiate the mechanical behaviors in these different parts. In other studies, conventionally, 3-point bending test was often performed on long bones (Caetano-Lopes et al., 2009; Vidal et al., 2018). It only measures the stiffness of diaphysis but cannot capture the mechanical behaviors of the joints.

Another advantage of mechanical testing coupled with micro-CT is that it can assess the mechanical behaviors inside the internal trabecular bone microstructures without sectioning the specimens. Whereas the conventional methods, such as strain gauges (Melville et al., 2015; Patel et al., 2014; De Souza et al., 2005) and digital image correlation (DIC) (Sztefek et al., 2010; Carriero et al., 2014; Amin Yavari et al., 2013) only measure the strain on external bone surfaces. Moreover, the bone morphology and mineral density assessment is sensitive to the selection of region-of-interest (ROI) and threshold in image segmentation (Bouxsein et al., 2010). However, the deformation and strain measured by mechanical testing coupled with micro-CT are not affected by the selection of region-of-interest, and no image segmentation was needed for the internal bone microstructure.

The mechanical testing coupled with micro-CT and the DVC method have been for strain mapping in trabecular bone blocks (Verhulp et al., 2004; Zauel et al., 2006), vertebra (Hussein et al., 2012), diaphysis of mouse tibia (Giorgi and Dall'Ara, 2018). In our prior works, we have used this method to map strain in native and implanted mandible (Du et al., 2015; Zhou et al., 2020a) and glenoid (Zhou et al., 2020b). To the best of our knowledge, in this study for the first time this method was used to focus on the localized deformation and strain measurement in mouse proximal tibia. The noise level was determined by the zero-load method to be much small than the measure deformation and strain. The results indicate that it is a valid method and can potentially be applied to study the small-scale mechanical behaviors inside mouse proximal tibia.

There are also some limitations in the methods used in the current work. The loading condition in the current study is not the same as the physiological loading conditions for mouse tibia (Gross et al., 2002), which would include bending as well as smaller contact area than that performed here. Nevertheless, the methods used in this study are valid for characterizing the stiffness of mouse tibia, especially the proximal tibia. Another weakness of this study is that the localized deformation and strain in proximal tibia were only measured in one typical specimen in each group, though the overall stiffness of mouse tibia was measured and reported for each specimen (n = 9 to 15). Thus, a systematic study with larger sample size and rigorous statistical analysis is recommended as a direction for future work. In the future, the mechanics theories of cellular materials (Gibson and Ashby, 1997) can be used to analyze the correlation of bone morphology and mineral density to mechanical behaviors of bone (Gibson and Ashby, 1997). Also, micro-CT based finite element analysis (Mao et al., 2019) can also be used to study the mechanical behaviors of CIA and GMSC-treated tibia computationally. Furthermore, this study only investigated the morphological and

mechanical tibia bone properties at one time point. Future work should include more time points to further investigate the progress of therapeutic effects and the mechanisms of GMSC treatment on CIA mice.

5. Conclusions

This paper presents the results of experimental measurements of microstructure and mechanical behaviors of tibia for GMSC-treated CIA mice. CIA disease caused bone erosion in epiphyseal cortical bone, which manifested into the adjacent epiphyseal trabecular bone, and also affected the metaphyseal cortical bone. CIA disease also weakened the load-bearing function of proximal tibia. GMSC treatment interfered with the progress of CIA disease, attenuated the bone erosion in epiphyseal and metaphyseal trabecular bone and resulted in improved load-bearing function of tibia. GMSCs provide a promising potential treatment of autoimmune arthritis.

CRediT authorship contribution statement

Y Zhou: Formal analysis, Methodology, Validation, Visualization, Writing – Original Draft; J Dang: Resources; Y Chen: Resources; SG Zheng: Conceptualization, Funding acquisition, Resources; J Du: Conceptualization, Funding acquisition, Methodology, Resources, Writing – Review & Editing.

Declaration of competing interest

The authors declare that they have no known competing financial interests or personal relationships that could have appeared to influence the work reported in this paper.

Appendix A. Supplementary data

Supplementary data to this article can be found online at https://doi.org/10.1016/j.jmbbm.2021.104719.

References

Aletaha, D., Smolen, J.S., 2018. Diagnosis and management of rheumatoid arthritis: a Review. JAMA, J. Am. Med. Assoc. https://doi.org/10.1001/jama.2018.13103.

Amin Yavari, S., van der Stok, J., Weinans, H., Zadpoor, A.A., 2013. Full-field strain measurement and fracture analysis of rat femora in compression test. J. Biomech. https://doi.org/10.1016/j.jbiomech.2013.02.007.

Bhushan, B., 2000. Surface roughness analysis and measurement techniques. In: Mod. Tribol. Handb. Vol. One Princ. Tribol., pp. 49–119. https://doi.org/10.1201/9780849377877.ch2

Bouxsein, M.L., Boyd, S.K., Christiansen, B.A., Guldberg, R.E., Jepsen, K.J., Müller, R., 2010. Guidelines for assessment of bone microstructure in rodents using micro-computed tomography. J. Bone Miner. Res. 25, 1468–1486. https://doi.org/10.1002/jbmr.141.

Caetano-Lopes, J., Nery, A.M., Henriques, R., Canhão, H., Duarte, J., Amaral, P.M., Vale, M., Moura, R.A., Pereira, P.A., Weinmann, P., Abdulghani, S., Souto-Carneiro, M., Rego, P., Monteiro, J., Sakagushi, S., Queiroz, M.V., Konttinen, Y.T., Graça, L., Vaz, M.F., Fonseca, J.E., 2009. Chronic arthritis directly induces quantitative and qualitative bone disturbances leading to compromised

biomechanical properties. Clin. Exp. Rheumatol. 27, 475–482. http://www.ncbi.nlm.nih.gov/pubmed/19604441.

Carriero, A., Abela, L., Pitsillides, A.A., Shefelbine, S.J., 2014. Ex vivo determination of bone tissue strains for an in vivo mouse tibial loading model. J. Biomech. https://doi.org/10.1016/j.jbiomech.2014.03.035.

Chen, M., Su, W., Lin, X., Guo, Z., Wang, J., Zhang, Q., Brand, D., Ryffel, B., Huang, J., Liu, Z., He, X., Le, A.D., Zheng, S.G., 2013. Adoptive transfer of human gingiva-derived mesenchymal stem cells ameliorates collagen-induced arthritis via suppression of Th1 and Th17 cells and enhancement of regulatory T cell differentiation. Arthritis Rheum. 65, 1181–1193. https://doi.org/10.1002/art.37894.

Chen, Y., Xu, Z., Liang, R., Wang, J., Xu, A., Na, N., Li, B., Wang, R., Joseph, M., Olsen, N., Hsueh, W., Zheng, S.G., 2020. CD4+CD126low/- Foxp3+ cell population represents a superior subset of regulatory T cells in treating autoimmune diseases. Mol. Ther. https://doi.org/10.1016/j.ymthe.2020.07.020.

Clarke, S.P., Moghaddam, N.G., das Nair, R., Walsh, D.A., Scammell, B., 2016. Psychological therapies for improving outcomes after total hip or knee replacement in people with osteoarthritis and rheumatoid arthritis. Cochrane Database Syst. Rev. https://doi.org/10.1002/14651858.CD012474.

De Souza, R.L., Matsuura, M., Eckstein, F., Rawlinson, S.C.F., Lanyon, L.E., Pitsillides, A. A., 2005. Non-invasive axial loading of mouse tibiae increases cortical bone formation and modifies trabecular organization: a new model to study cortical and cancellous compartments in a single loaded element. Bone. https://doi.org/10.1016/j.bone.2005.07.022.

Deaglio, S., Dwyer, K.M., Gao, W., Friedman, D., Usheva, A., Erat, A., Chen, J.-F., Enjyoji, K., Linden, J., Oukka, M., Kuchroo, V.K., Strom, T.B., Robson, S.C., 2007. Adenosine generation catalyzed by CD39 and CD73 expressed on regulatory T cells mediates immune suppression. J. Exp. Med. 204, 1257–1265. https://doi.org/10.1084/jem.20062512.

Doube, M., Kłosowski, M.M., Arganda-Carreras, I., Cordelières, F.P., Dougherty, R.P., Jackson, J.S., Schmid, B., Hutchinson, J.R., Shefelbine, S.J., 2010. BoneJ: free and extensible bone image analysis in ImageJ. Bone 47, 1076–1079. https://doi.org/10.1016/j.bone.2010.08.023.

Dougherty, R., Kunzelmann, K.-H., 2007. Computing local thickness of 3D structures with ImageJ. Microsc. Microanal. https://doi.org/10.1017/s1431927607074430.

Du, J., Lee, J.-H., Jang, A.T., Gu, A., Hossaini-Zadeh, M., Prevost, R., Curtis, D.A., Ho, S. P., 2015. Biomechanics and strain mapping in bone as related to immediately-loaded dental implants. J. Biomech. 48, 3486–3494. https://doi.org/10.1016/j.jbiomech.2015.05.014.

Firestein, G.S., 2003. Evolving concepts of rheumatoid arthritis. Nature 423, 356–361. https://doi.org/10.1038/nature01661.

Frey, O., Reichel, A., Bonhagen, K., Morawietz, L., Rauchhaus, U., Kamradt, T., 2010. Regulatory T cells control the transition from acute into chronic inflammation in glucose-6-phosphate isomerase-induced arthritis. Ann. Rheum. Dis. 69, 1511–1518. https://doi.org/10.1136/ard.2009.123422.

Gibson, L.J., Ashby, M.F., 1997. Cellular Solids. Cambridge University Press, Cambridge. https://doi.org/10.1017/CBO9781139878326.

Giorgi, M., Dall'Ara, E., 2018. Variability in strain distribution in the mice tibia loading model: a preliminary study using digital volume correlation. Med. Eng. Phys. 62, 7–16. https://doi.org/10.1016/j.medengphy.2018.09.001.

Goldring, S.R., Gravallese, E.M., 2000. Pathogenesis of bone erosions in rheumatoid arthritis. Curr. Opin. Rheumatol. 12, 195–199. https://doi.org/10.1097/00002281-200005000-00006.

Gross, T.S., Srinivasan, S., Liu, C.C., Clemens, T.L., Bain, S.D., 2002. Noninvasive loading of the murine tibia: an in vivo model for the study of mechanotransduction. J. Bone Miner. Res. 17, 493–501. https://doi.org/10.1359/jbmr.2002.17.3.493.

Helmick, C.G., Felson, D.T., Lawrence, R.C., Gabriel, S., Hirsch, R., Kwoh, C.K., Liang, M. H., Kremers, H.M., Mayes, M.D., Merkel, P.A., Pillemer, S.R., Reveille, J.D., Stone, J. H., 2008. Estimates of the prevalence of arthritis and other rheumatic conditions in the United States: Part I. Arthritis Rheum. 58, 15–25. https://doi.org/10.1002/art.23177.

Hermann, K.-G.A., Backhaus, M., Schneider, U., Labs, K., Loreck, D., Zühlsdorf, S., Schink, T., Fischer, T., Hamm, B., Bollow, M., 2003. Rheumatoid arthritis of the shoulder joint: comparison of conventional radiography, ultrasound, and dynamic contrast-enhanced magnetic resonance imaging. Arthritis Rheum. 48, 3338–3349. https://doi.org/10.1002/art.11349.

Hussein, A.I., Barbone, P.E., Morgan, E.F., 2012. Digital volume correlation for study of the mechanics of whole bones. Procedia IUTAM 4, 116–125. https://doi.org/10.1016/j.piutam.2012.05.013.

Kelly, I.G., Foster, R.S., Fisher, W.D., 1987. Neer total shoulder replacement in rheumatoid arthritis. J. Bone Joint Surg. Br. 69, 723–726. https://doi.org/10.1302/0301-620X.69B5.3680331.

Kirwan, J.R., Currey, H.L., Freeman, M.A., Snow, S., Young, P.J., 1994. Overall long-term impact of total hip and knee joint replacement surgery on patients with osteoarthritis and rheumatoid arthritis. Br. J. Rheumatol. 33, 357–360. https://doi.org/10.1093/rheumatology/33.4.357.

Lan, Q., Fan, H., Quesniaux, V., Ryffel, B., Liu, Z., Zheng, S.G., 2012. Induced Foxp3(+) regulatory T cells: a potential new weapon to treat autoimmune and inflammatory diseases? J. Mol. Cell Biol. 4, 22–28. https://doi.org/10.1093/jmcb/mjr039.

Lee, J.K., Choi, C.-H., 2012. Total knee arthroplasty in rheumatoid arthritis. Knee Surg. Relat. Res. 24, 1–6. https://doi.org/10.5792/ksrr.2012.24.1.1.

Lee, D.M., Weinblatt, M.E., 2001. Rheumatoid arthritis. Lancet (London, England) 358, 903–911. https://doi.org/10.1016/S0140-6736(01)06075-5.

Lereim, P., Goldie, I.F., 1975. Relationship between morphologic features and hardness of the subchondral bone of the medial tibial condyle in the normal state and in osteoarthritis and rheumatoid arthritis. Arch. Orthop. Unfall-Chir. 81, 1–11. https://doi.org/10.1007/BF00417022.

Lereim, P., Goldie, I., Dahlberg, E., 1974. Hardness of the subchondral bone of the tibial condyles in the normal state and in osteoarthritis and rheumatoid arthritis. Acta Orthop. 45, 614–627. https://doi.org/10.3109/17453677408989184.

Lindqvist, E., 2002. Ten year outcome in a cohort of patients with early rheumatoid arthritis: health status, disease process, and damage. Ann. Rheum. Dis. 61, 1055–1059. https://doi.org/10.1136/ard.61.12.1055.

Luo, Y., Wu, W., Gu, J., Zhang, X., Dang, J., Wang, J., Zheng, Y., Huang, F., Yuan, J., Xue, Y., Fu, Q., Kandalam, U., Colello, J., Zheng, S.G., 2019. Human gingival tissue-derived MSC suppress osteoclastogenesis and bone erosion via CD39-adenosine signal pathway in autoimmune arthritis. EBioMedicine. https://doi.org/10.1016/j.ebiom.2019.04.058.

Mao, Q., Su, K., Zhou, Y., Hossaini-Zadeh, M., Lewis, G.S., Du, J., 2019. Voxel-based micro-finite element analysis of dental implants in a human cadaveric mandible: tissue modulus assignment and sensitivity analyses. J. Mech. Behav. Biomed. Mater. 94, 229–237. https://doi.org/10.1016/j.jmbbm.2019.03.008.

Melville, K.M., Robling, A.G., van der Meulen, M.C.H., 2015. In vivo axial loading of the mouse tibia. Methods Mol. Biol. https://doi.org/10.1007/978-1-4939-1619-1_9.

Ott, S.M., 2018. Cortical or trabecular bone: what's the difference? Am. J. Nephrol. 47, 373–375. https://doi.org/10.1159/000489672.

Patel, T.K., Brodt, M.D., Silva, M.J., 2014. Experimental and finite element analysis of strains induced by axial tibial compression in young-adult and old female C57Bl/6 mice. J. Biomech. 47, 451–457. https://doi.org/10.1016/j.jbiomech.2013.10.052.

Perhala, R.S., Wilke, W.S., Clough, J.D., Segal, A.M., 1991. Local infectious complications following large joint replacement in rheumatoid arthritis patients treated with methotrexate versus those not treated with methotrexate. Arthritis Rheum. 34, 146–152. https://doi.org/10.1002/art.1780340204.

Rittmeister, M., Kerschbaumer, F., 2001. Grammont reverse total shoulder arthroplasty in patients with rheumatoid arthritis and nonreconstructible rotator cuff lesions. J. Shoulder Elbow Surg. 10, 17–22. https://doi.org/10.1067/mse.2001.110515.

Sakaguchi, S., Yamaguchi, T., Nomura, T., Ono, M., 2008. Regulatory T cells and immune tolerance. Cell 133, 775–787. https://doi.org/10.1016/j.cell.2008.05.009.

Schett, G., Gravallese, E., 2012. Bone erosion in rheumatoid arthritis: mechanisms, diagnosis and treatment. Nat. Rev. Rheumatol. 8, 656–664. https://doi.org/10.1038/nrrheum.2012.153.

Silva, M.D., Ruan, J., Siebert, E., Savinainen, A., Jaffee, B., Schopf, L., Chandra, S., 2006. Application of surface roughness analysis on micro-computed tomographic images of bone erosion: examples using a rodent model of rheumatoid arthritis. Mol. Imag. https://doi.org/10.2310/7290.2006.00025.

Sztefek, P., Vanleene, M., Olsson, R., Collinson, R., Pitsillides, A.A., Shefelbine, S., 2010. Using digital image correlation to determine bone surface strains during loading and after adaptation of the mouse tibia. J. Biomech. 43, 599–605. https://doi.org/10.1016/j.jbiomech.2009.10.042.

Trentham, D.E., Townes, A.S., Kang, A.H., 1977. Autoimmunity to type II collagen an experimental model of arthritis. J. Exp. Med. 146, 857–868. https://doi.org/10.1084/jem.146.3.857.

Verhulp, E., Van Rietbergen, B., Huiskes, R., 2004. A three-dimensional digital image correlation technique for strain measurements in microstructures. Exp. Mech. 37, 1313–1320. https://doi.org/10.1016/j.jbiomech.2003.12.036.

Vidal, B., Cascão, R., Finnilä, M.A.J., Lopes, I.P., Saarakkala, S., Zioupos, P., Canhão, H., Fonseca, J.E., 2018. Early arthritis induces disturbances at bone nanostructural level reflected in decreased tissue hardness in an animal model of arthritis. PloS One 13, e0190920. https://doi.org/10.1371/journal.pone.0190920.

Yang, J.P., Bogoch, E.R., Woodside, T.D., Hearn, T.C., 1997. Stiffness of trabecular bone of the tibial plateau in patients with rheumatoid arthritis of the knee. J. Arthroplasty 12, 798–803. https://doi.org/10.1016/S0883-5403(97)90011-5.

Zauel, R., Yeni, Y.N., Bay, B.K., Dong, X.N., Fyhrie, D.P., 2006. Comparison of the linear finite element prediction of deformation and strain of human cancellous bone to 3D digital volume correlation measurements. J. Biomech. Eng. 128, 1–6. https://doi.org/10.1115/1.2146001.

Zheng, S.G., Wang, J.H., Koss, M.N., Quismorio, F., Gray, J.D., Horwitz, D.A., 2004a. CD4+ and CD8+ regulatory T cells generated ex vivo with IL-2 and TGF-beta suppress a stimulatory graft-versus-host disease with a lupus-like syndrome. J. Immunol. 172, 1531–9. http://www.ncbi.nlm.nih.gov/pubmed/14734731.

Zheng, S.G., Wang, J.H., Gray, J.D., Soucier, H., Horwitz, D.A., 2004b. Natural and induced CD4+CD25+ cells educate CD4+CD25- cells to develop suppressive activity: the role of IL-2, TGF-beta, and IL-10. J. Immunol. 172, 5213–5221.

Zhou, X., Kong, N., Wang, J., Fan, H., Zou, H., Horwitz, D., Brand, D., Liu, Z., Zheng, S.G., 2010. Cutting edge: all-trans retinoic acid sustains the stability and function of natural regulatory T cells in an inflammatory milieu. J. Immunol. 185, 2675–2679. https://doi.org/10.4049/jimmunol.1000598.

Zhou, Y., Gong, C., Hossaini-Zadeh, M., Du, J., 2020a. 3D full-field strain in bone-implant and bone-tooth constructs and their morphological influential factors. J. Mech. Behav. Biomed. Mater. https://doi.org/10.1016/j.jmbbm.2020.103858.

Zhou, Y., Gong, C., Lewis, G.S., Armstrong, A.D., Du, J., 2020b. 3D full-field biomechanical testing of a glenoid before and after implant placement. Extrem. Mech. Lett. 35, 100614. https://doi.org/10.1016/j.eml.2019.100614.